

THREE-DIMENSIONAL STRUCTURAL ASPECTS OF THE ATTACHED TURBULENT BOUNDARY LAYER FLOW OVER A HILL

Julie E. Duetsch-Patel, Aldo Gargiulo, William J. Devenport, and K. Todd Lowe

Kevin T. Crofton Department of Aerospace and Ocean Engineering
Virginia Tech

Blacksburg, VA, 24060, USA

jduetsch@vt.edu, galdo@vt.edu, devenport@vt.edu, kelowe@vt.edu

ABSTRACT

The BeVERLI (Benchmark Validation Experiments for RANS/LES Investigations) Hill bump model, designed specifically for validation experiments, was tested in the Virginia Tech Stability Wind Tunnel to collect validation experiment data on the three-dimensional (3D) boundary layer flow over a 3D hill. Laser Doppler velocimetry measurements on the bump model were used to study the mean flow and turbulence structure and evaluate the impact of pressure gradient and curvature upon the total shear stress in the boundary layer and evaluate the impact of pressure gradient and curvature upon the total shear stress behavior in the near-wall region. From analysis of the BeVERLI Hill flow, including the boundary layer just upstream of the hill, and comparison with the 3D flow around a wing-body junction of Ölçmen *et al.* (2001), it is shown that there is no region in which the total shear stress is approximately constant, unlike the typical behavior for 2D equilibrium flows.

INTRODUCTION

Among the most well-known features of three-dimensional turbulent boundary layers (3D TBLs) are the lag between the shear-stress direction vector and the velocity-gradient vector direction, a reduction in near-wall turbulent kinetic energy and Reynolds stresses, and a reduction in the turbulence parameter A_1 below its typical 2D value of 0.15. Because of this, 3D TBLs present a particular challenge to modeling, as the stress/strain misalignment invalidates the assumptions behind any turbulence models that assume an isotropic eddy viscosity. This limits the utility of Reynolds-Averaged Navier Stokes (RANS) computational fluid dynamics (CFD) for flows of engineering interest, even as CFD is increasingly used for high-impact decisions in vehicle design. Improved modeling of 3D flows depends upon a better understanding of 3D boundary layers and turbulence to improve the assumptions that go into turbulence models.

The flow over a wall-mounted bump is a common test case to the goal of improved computational fidelity (e.g. Byun & Simpson (2006); Bell *et al.* (2012)), as the simple geometry generates a flow field with pressure gradient, curvature effects, and three-dimensional boundary layer separation and reattachment. All these features are generally challenging for CFD and are very common in practical applications.

Unlike RANS, large-eddy simulation (LES) resolves the larger turbulence scales and models the small scales that cannot be resolved on the grid. As a result, LES requires a sub-

grid scale (SGS) model to model the effects of the small scales on the resolved flow. Accurately resolving or modeling near-wall motions is critical because production, dissipation, turbulent kinetic energy, and Reynolds-stress anisotropy all peak below $x_2^+ = 20$, and as such, all meshes and filtering for LES must be on the order of one viscous unit. Because of this, wall-resolved LES is infeasible for higher Reynolds number applications, requiring wall-modeled LES. Like RANS turbulence models, existing wall models are largely built on equilibrium assumptions, which are not valid in the vast majority of applicable 3D flows. These assumptions can be built into the model directly, for example through assuming an equilibrium stress or velocity distribution, or indirectly through assumptions regarding eddy viscosity and inner-layer Reynolds stress.

Equilibrium two-dimensional boundary layers typically have a region near the wall where the total shear stress is nearly constant, approximately $0.95 \leq \tau_{total}/\tau_w \leq 1$ for sufficiently high Reynolds numbers. Devenport & Lowe (2022) demonstrate the derivation of 2D zero-pressure gradient boundary layer equations that produce this behavior, showing that as the viscous shear stress decreases rapidly outside the viscous sub-layer, the turbulent shear stress increases to balance out the total shear stress. In non-zero pressure gradient flows, a linear gradient of the total shear stress will be present instead.

Equilibrium approximations to the thin-boundary layer equations are often made to relax strict assumptions on the velocity profile that would otherwise be required for LES (Bose & Park (2018)). These approximations also lead to the assumption of a constant total stress region in the near-wall region of the boundary layer. However, most flows of engineering interest involve strong pressure gradients in both the streamwise and lateral direction and other non-equilibrium phenomena, which will invalidate these assumptions.

This work presents results from experiments studying the three-dimensional turbulent attached and separated flow over the BeVERLI (Benchmark Validation Experiment for RANS/LES Investigations) Hill. The flow over this model experiences three-dimensional pressure gradients of varying sign and magnitude and skewing and three-dimensional flow effects. We study the evolution of the boundary layer from upstream of the hill to over the hill itself, specifically the impact of curvature, 3D pressure gradients, and skewing upon the total shear stress distribution in the boundary layer. It will be shown that streamwise and lateral pressure gradients and skewing significantly impact the flow, reducing the turbulent shear stress throughout the boundary layer and resulting in no constant shear stress region for any of the stations studied.

Table 1. LDV data locations of interest for this study, focusing on Windward (W) stations. $\Pi_{WSS} = (\partial C_p / \partial x_3) \Big|_{WSS} / (\partial C_p / \partial x_1) \Big|_{WSS}$ is the ratio of pressure gradients in local wall-shear-stress coordinates at $Re_H = 250,000$, γ_{FA} is the mean flow angle closest to the wall relative to the global x_1 axis, δ_0/R is the ratio of the empty tunnel boundary layer thickness at the location of the bump height to the magnitude of the local radius of curvature at each station, and $\beta_{X_i} = (\delta_{inflow}^* / \tau_{w,inflow}) (\partial P / \partial X_i)$ is the Clauser parameter.

Station	x_1/H	x_2/H	x_3/H	u_τ/U_∞	Min x_2^+	Max x_2^+	γ_{FA} ($^\circ$)	$\delta_0/ R $	Π_{WSS}	β_{X_1}	β_{X_3}
W1	-4.1	0	0	0.034	3.8	919	0	0	0	1.3	0
W2	-1.55	0.02	-1.55	0.037	5.3	1209	-38.9	0.38	-0.02	-3.1	0.9
W3	-1.42	0.07	-1.42	0.038	2.0	1510	-37.4	0.36	-0.10	-1.7	2.4
W5	-0.80	0.70	-0.80	0.043	4.3	1683	16.0	0.12	-3.3	-4.4	5.4

EXPERIMENTAL SETUP

Measurements were performed in the Virginia Tech Stability Wind Tunnel (SWT) in a configuration as depicted in Fig. 1. The bump geometry is defined by Gargiulo *et al.* (2020) and, from the two-dimensional view, consists of a mirrored fifth-degree polynomial with a flat top in between. The model has a length of 0.93472 m and a height of 0.1869 m and exhibits 90 degree rotational symmetry, allowing for different orientations of the model with respect to the incoming flow. For these experiments, the bump was oriented as shown in Fig. 1 with a pair of rounded corners directly aligned with the approaching freestream. This orientation is referred to as the 45° yaw case (Gargiulo *et al.* (2020)). Coordinate systems labeled X_i indicate global coordinates, with the origin at the center of the hill, while coordinate systems labeled lowercase x_i indicate local wall-shear-stress coordinates, with the origin at the wall-location of the profile.

Two CNC-milled models were used: One with 135 pressure taps installed in the surface and one with slots for clear windows for laser Doppler velocimetry (LDV) measurements along the fifth-degree polynomial curves. The models were scanned after manufacturing and found to match the design geometry to within ± 0.40 mm and ± 0.30 mm, respectively.

The model was installed 6.88 m downstream of the 3.18 mm boundary layer trip in the wind tunnel contraction. Near the inflow to the test section, 1.83 m upstream of the center of the hill ($X_1/H = -9.8$, $X_3/H = 0$), the boundary layer has $\delta_{99} = 5.7$ cm, $\delta^* = 0.87$ cm, and $\theta = 0.65$ cm such that $Re_\theta = 8615$ and $Re_\tau = 2763$. Measurements were made with the freestream flow adjusted to ensure height-based Reynolds numbers Re_H of $250,000 \pm 5000$ and $325,000 \pm 5000$. Without the bump present, the boundary layer thickness at the location of the center of the bump is approximately 7.3 cm at $Re_H \approx 325,000$. Measurements collected at $Re_H = 250,000$ are the focus of this study.

A specialized embedded three-component LDV system was used to take measurements of the turbulent boundary layer over the bump surface and upstream of the model, as shown in Fig. 2. The probe was mounted inside the bump, with the laser beams passing through the 1.5mm anti-reflective curvature-fitting acrylic windows. The Doppler frequency signals are obtained using AURStudio from AUR, Inc. One block of samples (ranging from 5,000 to 15,000 samples) was taken at each measurement point above the wall. Near-wall points were collected over approximately one minute of sampling time to prevent seed particles from collecting on the acrylic windows, and thus typically had fewer samples than points taken above $x_2 \approx 0.5$ mm. Data further above the surface was collected over approximately one to three minutes of sampling time.

During post-processing, outlying points from histograms were removed. Nominal x_2 -heights at each point in the profile were corrected by fitting the nearest-wall data to $U_1^+ = x_2^+$ for data in the linear sublayer. The measurement volume was approximately 45 μ m in diameter, and measurements were achievable at a minimum and maximum height above the wall of 0.1 mm and 30 mm, respectively. The flow was seeded using a mineral oil smoke machine (MDG MAX 3000 APS) with particles ranging in size from 0.5 to 1 μ m, resulting in Stokes numbers small enough to capture the full range of relevant scales.

Data was collected at 13 locations on the bump surface, as well as at the inflow to the test section and on the flat wall just upstream of the hill. For this study, four locations are of interest at $Re_H = 250,000$, as shown in Table 1, where Π_{WSS} is the pressure-gradient ratio parameter in local wall-shear-stress coordinates proposed by Lozano-Durán *et al.* (2020) to assess the degree to which the flow is non-equilibrium. These selected stations all contain data in the linear sublayer, allowing for a direct calculation of τ_w from the velocity gradient.

Instrumentation and statistical uncertainty of the results are $\delta(U_1/U_\infty) = 0.012$, $\delta(U_2/U_\infty) = 0.007$, $\delta(U_3/U_\infty) = 0.010$, $\delta(\overline{u_1^2}/U_\infty^2) = 1.2 \times 10^{-3}$, $\delta(\overline{u_2^2}/U_\infty^2) = 3.0 \times 10^{-4}$, $\delta(\overline{u_3^2}/U_\infty^2) = 1.7 \times 10^{-3}$, $\delta(\overline{u_1 u_2}/U_\infty^2) = 8.1 \times 10^{-5}$, $\delta(\overline{u_1 u_3}/U_\infty^2) = 7.1 \times 10^{-4}$, and $\delta(\overline{u_2 u_3}/U_\infty^2) = 3.2 \times 10^{-4}$. Rigorous uncertainty quantification encompassing additional uncertainty sources (e.g. article geometry uncertainty effects and repeatability of measurements) is critical for the BeVERLI Hill experiments to ensure the results are suitable for CFD validation. Further depth of uncertainty estimations will be provided in future publications.

RESULTS

Pressure Distribution

Fig. 2(a) shows the mean freestream pressure coefficient contours over the entire hill at a 45° orientation at $Re_H = 250,000$. As shown, the pressure gradient changes sign multiple times over the surface in both the streamwise and spanwise directions as the flow away from the centerline is accelerated around the sides of the model. These strong streamwise and spanwise pressure gradients and 3D curvature induce strong near-wall crossflow. LDV profile locations are indicated by the black circles. The four stations of interest for this study are labeled. Fig. 2(b) shows a focus view of the stations of interest on the hill, including wall-shear stress direction (from the mean flow angle) indicated by black vectors, and the mean flow direction $x_2^+ \approx 500$ indicated by blue vectors. The maximum x_2^+ captured at each profile is given in Table 1.

The flow begins largely two-dimensional in an adverse

pressure gradient (APG) at station W1. As the flow approaches the hill, the APG increases in strength up to the stagnation region on the front of the model, after which it is accelerated over the windward face of the hill. Along the sides, stations W2 and W3 experience similar pressure gradients and pressure gradient histories. At these stations, the flow direction next to the wall is inclined nearly 40° relative to the upstream flow direction, indicating strong skewing under the lateral pressure gradients present upstream of these stations.

In contrast, station W5 experiences an entirely different pressure gradient and pressure gradient history. The local streamwise pressure gradient remains favorable, as the near-wall flow direction remains nearly perpendicular to the local pressure coefficient contours. However, the lateral pressure gradients have induced milder skewing, pointing in the opposite direction relative to the skewing at W2 and W3. Here, the flow direction next to the wall is inclined 16° relative to the upstream flow direction.

Mean Velocity and Turbulence

LDV measurements were collected in global tunnel coordinates, as shown in Fig. 1, and transformed into local wall-shear-stress coordinates for analysis. In this coordinate system, the x_1 -axis points in the estimated direction of the wall-shear stress vector at the wall via the mean flow angle closest to the surface, indicated in Fig. 2(b) by black arrows. The x_2 -axis is perpendicular to the local surface curvature, and the x_3 -axis completes a right-handed coordinate system.

As shown in Fig. 3, the flow begins largely 2D with near-zero components in U_2 and U_3 at W1. However, the flow experiences vastly different physics in different regions over the BeVERLI Hill, with varying levels of skewing and streamwise acceleration depending on the location on the model, as discussed. Though the U_2 and U_3 components are near-zero near the wall due to the wall-shear-stress coordinate system, the U_3 components for all stations on the bump increase significantly further away from the surface due to the flow skewing. The U_2 components are near-zero for all profiles, although all profiles on the hill experience a small, increasingly negative component of U_2 as a function of height above the surface, especially at Station W5. This could be due to the local pressure gradient acting to pull the freestream flow down towards the surface at this station as it negotiates the turn over the hill.

The behavior in the Reynolds stresses in Figs. 4 and 5 is even more varied between stations. Select Reynolds stress components are shown in Fig. 5 normalized on the friction velocity for comparison with equilibrium 2D TBL behavior. The $\overline{u'_1 u'_3}/U_\infty^2$ and $\overline{u'_2 u'_3}/U_\infty^2$ are approximately zero within uncertainties. Unexpectedly, the flow at W1 does not behave like a typical 2D APG, as seen when compared to the zero-pressure gradient (ZPG) direct numerical simulation (DNS) data of Schlatter & Örlü (2010) in Fig. 5, as the inner peak decreases in magnitude instead of rising above the 2D ZPG level and $\overline{u'_1 u'_2}/U_\infty^2$ decreases in magnitude relative to the ZPG DNS. Further work is needed to explain this discrepancy.

In contrast, all three stations on the bump have significant components of both normal and shear stresses. Stations W2 and W3, located near each other and in a region of similar pressure gradient and pressure gradient histories, experience very similar turbulence behavior, as well as significant skewing of the near-wall flow relative to the tunnel X_1 -axis and local concave curvature (see Figure 6). While concave curvature generally has a destabilizing effect on a 2D TBL, Baskaran *et al.* (1990) found that the combined effects of mild convex and concave curvature and mean flow three-dimensionality were

small compared to the impact of those two parameters when applied individually. The behavior between the stations primarily differs in $\overline{u'_1 u'_2}/U_\infty^2$. The inner-region peak in $\overline{u'_1 u'_2}/U_\infty^2$ is not captured at station W2, and the behavior after the peak is lower in magnitude than at nearby station W3.

Station W5 experiences very different turbulence behavior than the other stations due to the different flow histories, pressure gradients, and local curvature in this region. Here, the flow most notably experiences a decrease in the peak of $\overline{u'_1 u'_2}/U_\infty^2$, a sharp increase in the magnitude of $\overline{u'_3 u'_3}/U_\infty^2$, and an inflection point in $\overline{u'_1 u'_2}/U_\infty^2$ in the log layer. This behavior is likely due to the skewed near-wall flow interacting with the flow at the edge of the boundary layer, which is probably nearly aligned with the wind tunnel freestream direction.

Total Shear Stress

In the wall-shear stress coordinate system, the total shear stress is composed of the viscous component, $\mu \partial U_1 / \partial x_2$, which is maximum in the viscous sublayer, and the turbulent component, $\rho (\overline{u'_1 u'_2}^2 + \overline{u'_2 u'_3}^2)^{1/2}$. The wall-parallel momentum equations can be simplified to focus upon the behavior of the flow in the limit of being in wall-shear-stress coordinates in the viscous sublayer by ignoring the inertial terms and Reynolds shear stresses, resulting in $U_1^+ = \frac{\partial P^+}{\partial x_1^+} \frac{x_2^{+2}}{2} + x_2^+$ and $U_3^+ = \frac{\partial P^+}{\partial x_3^+} \frac{x_2^{+2}}{2}$. If the pressure gradient is assumed to be approximately constant as a function of height in the viscous sublayer, then an FPG will cause the viscous stress to reduce more rapidly from the wall in wall units than a ZPG or APG due to the influence of the pressure term.

The turbulent shear stress is also very sensitive to flow conditions. The presence of mean streamwise vorticity is known to impact the quasi-coherent turbulent structures that are responsible for the production of $\overline{u'_1 u'_2}$ and $\overline{u'_2 u'_3}$ (Johnston & Flack (1996)) and lead to the reduction of these shear stress components. However, Flack & Johnston (1998) have also found that $\tau_{turbulent}$ increases outside of the buffer layer in regions of increasing three-dimensionality. This can also be seen at some stations in the data of Ölgmen *et al.* (2001). For both experiments, although $\overline{u'_1 u'_2}$ decreased in magnitude as the three-dimensionality of the flow increased, an increase in the magnitude of $\overline{u'_2 u'_3}$ compensated for this behavior and led to an increase in $\tau_{turbulent}$ outside of the buffer layer.

The viscous and turbulent shear stress components of the total shear stress in the BeVERLI Hill stations of interest are normalized by τ_w , computed via u_τ , in Fig. 7 and compared with the 2D ZPG equilibrium boundary layer DNS of Schlatter & Örlü (2010). As shown in Fig. 7, stations W2 and W3 both experience a region below $x_2^+ \approx 200$ where the turbulent shear stress is significantly reduced and not able to balance out the viscous stress it drops outside of the linear sublayer. This results in a total stress distribution that is far from the equilibrium $0.95 \leq \tau/\tau_w \leq 1$ that is typically present in 2D ZPG boundary layers and is assumed in some turbulence models. Above $x_2^+ \approx 200$, there is a sharp increase in the turbulent stress, as was also observed by Flack & Johnston (1998) (though in their case, this was observed above $x_2^+ \approx 50$). There is, therefore, a region below $x_2^+ \approx 200$ that is dominated by viscous and wall-effects, and a region above this point of the boundary layer where the effects of the crossflow stress $\overline{u'_2 u'_3}$ begin to contribute more significantly as the flow turns away from the local wall-shear-stress direction. At Stations W2 and W3, this significant drop in turbulent shear stress is expected, as a reduction in turbulent shear stress is often seen

in 3D flows, where the significant near-wall skewing results suppresses the pressure-strain term in the turbulent transport.

In contrast, at station W5, the flow behavior is extremely different due to the different pressure gradient and flow history in this region. Notably, there is a small region near the wall where the turbulent shear stress approximately matches the 2D equilibrium DNS profile. This continues until the edge of the buffer layer, after which the shear stresses decrease for a portion of the log layer before sharply increasing again, similar to stations W2 and W3. This behavior near the wall may be due to the favorable streamwise pressure gradient in this region, the largest magnitude out of all of the stations. FPGs typically suppress turbulent fluctuations relative to the wall-shear-stress, including $\overline{u_1' u_2'}$ (e.g. Volino (2020)). However, in this case, the strong streamwise FPGs may accelerate the near-wall flow such that spanwise motions are inhibited, reducing the mean streamwise vorticity and near-wall three-dimensionality such that $\overline{u_1' u_2'}$ recovers in the near-wall region.

The profiles are compared in Fig. 8 with the 3D TBL on a flat wall around a wing-body junction from Ölçmen *et al.* (2001) in regions that experience similar pressure gradient and skewing behavior. At Stations 3 and 4 of Ölçmen *et al.*, the flow is extremely skewed ($> 30^\circ$ from the upstream flow direction), and streamwise pressure gradient is favorable as it passes around the side of the wing-body junction. This global flowfield behavior is similar to that of stations W2 and W3 of the BeVERLI flow, and, as shown, results in similar turbulent shear stress behavior, as shown in Fig. 8(a). However, the data of Ölçmen *et al.* is missing in the region in which Stations W2 and W3 begin experiencing a sharp increasing in the turbulent shear stress, so it is not possible to identify if this behavior is also present in the juncture flow.

A similar trend follows for Ölçmen *et al.*'s stations 6 and 7 and the hill's station W5. At both stations, the flow is much less skewed than at previous stations as it recovers past the junction and is also experiencing a stronger streamwise FPG than further upstream in the flow, similar to W5. Notably, all three stations experience a region through the buffer layer where the turbulent shear stress nearly matches the 2D DNS, before all show a sudden drop in turbulent shear stress above the buffer layer, and a subsequent increase in above $x_2^+ \approx 200$. Here, the effects of less severe near-wall skewing relative to the upstream flow direction, as well as very strong streamwise FPGs, may inhibit the mean streamwise vorticity such that the turbulent shear stresses recover locally in this region.

CONCLUSION

LDV measurements of the flow upstream of and on the three-dimensional BeVERLI Hill model were used to analyze the fluid physics at those stations. As shown, the selected stations experience significantly different mean flow and turbulence behavior due to differing pressure gradients, radii of curvature, and history effects at each station. Of these effects, local pressure gradient and skewing appear to be the strongest influences on the turbulence at each station.

Analysis of the BeVERLI Hill data and comparison with the 3D TBL on a flat wall around a wing-body junction from Ölçmen *et al.* (2001) show there is no region in the flow over the BeVERLI Hill where equilibrium assumptions regarding the shear stress distribution are valid. This is especially severe in strongly skewed flow, such as at stations W2 and W3. In accelerated regions of the flow with milder flow skewing, such as at station W5, the turbulent stresses below the buffer layer may approximately follow an equilibrium distribution, before diverging significantly from this behavior above $x_2^+ \approx 30$. Sim-

ilar behavior seen in the BeVERLI Hill flow was also observed in the flat wall flow around a wing-body juncture of Ölçmen *et al.* (2001) in regions with similar skewing and pressure gradient behavior. Turbulence models that rely on this equilibrium shear stress assumption will not be able to accurately predict the behavior of 3D flow.

ACKNOWLEDGEMENTS

The authors thank BeVERLI collaborators Vignesh Sundarraj, Tom Hallock, Thomas Ozoroski, Dr. Chris Roy, and Dr. Aurelien Borgoltz for their assistance with wind tunnel testing and thoughtful discussion on the data presented. We also thank NASA, particularly Dr. Michael Kegerise, Dr. Mujeeb Malik, and Dr. Christopher Rumsey, for their support under grants 80NSSC18M0146 and 80NSSC22M0061 and the Aerospace and Ocean Engineering Machine Shop staff for leading the fabrication and instrumentation hardware efforts.

REFERENCES

- Baskaran, V, Pontikis, Y G & Bradshaw, P 1990 Experimental investigation of three-dimensional turbulent boundary layers on 'infinite' swept wings. *J. Fluid Mech* **211**, 95–122.
- Bell, James H, Heineck, James T, Zilliac, Gregory, Mehta, Ra-bindra D & Long, Kurtis R 2012 Surface and flow field measurements on the FAITH hill model. In *50th AIAA Aerospace Sciences Meeting*, pp. 2012–0704. Nashville, TN: American Institute of Aeronautics and Astronautics.
- Bose, Sanjeeb T. & Park, George Ilhwan 2018 Wall-Modeled Large-Eddy Simulation for Complex Turbulent Flows. *Annual Review of Fluid Mechanics* **50**, 535–561.
- Byun, Gwibo & Simpson, Roger L. 2006 Structure of Three-Dimensional Separated Flow on an Axisymmetric Bump. *AIAA Journal* **44** (5), 999–1008.
- Devenport, William J. & Lowe, K. Todd 2022 Equilibrium and non-equilibrium turbulent boundary layers. *Progress in Aerospace Sciences* **131** (100807), 1–50.
- Flack, K. A. & Johnston, J. P. 1998 Near-wall flow in a three-dimensional boundary layer on the endwall of a 30° bend. *Experiments in Fluids* **24**, 175–184.
- Gargiulo, Aldo, Vishwanathan, Vidya, Fritsch, Daniel J, Duetsch-Patel, Julie E, Szoke, Mate, Borgoltz, Aurelien, Devenport, William J, Roy, Christopher J & Lowe, Kevin T 2020 Examination of Flow Sensitivities in Turbulence Model Validation Experiments. In *AIAA SciTech 2020 Forum*, pp. 2020–1583. Orlando.
- Johnston, J. P. & Flack, K. A. 1996 Review - Advances in Three-Dimensional Turbulent Boundary Layers With Emphasis on the Wall-Layer Regions. *Journal of Fluids Engineering* **118**, 219–232.
- Lozano-Durán, Adrián, Giometto, Marco G., Park, George Ilhwan & Moin, Parviz 2020 Non-equilibrium three-dimensional boundary layers at moderate Reynolds numbers. *Journal of Fluid Mechanics* **883** (A20), 1–42.
- Ölçmen, S M, Simpson, R L & George, J 2001 Some Reynolds number effects on two-and three-dimensional turbulent boundary layers. *Experiments in Fluids* **31**, 219–228.
- Schlatter, Philipp & Örlü, Ramis 2010 Assessment of direct numerical simulation data of turbulent boundary layers. *Journal of Fluid Mechanics* **659**, 116–126.
- Volino, Ralph J 2020 Turbulence structure in non-equilibrium boundary layers with favorable and adverse pressure gradients. *International Journal of Heat and Fluid Flow* **86**.

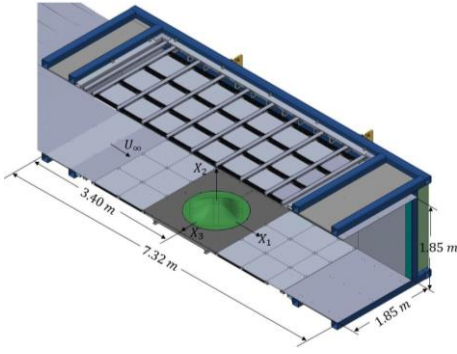


Figure 1. BeVERLI Hill geometry and global coordinate system. The side wall is shown as the floor to accurately portray the right-handed coordinate system.

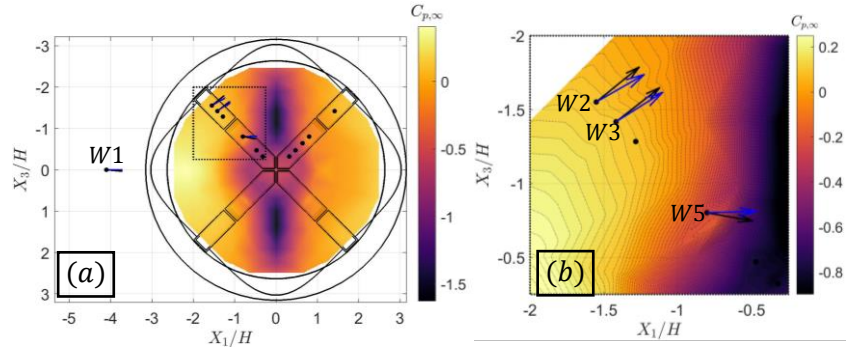


Figure 2. Freestream pressure coefficient contours over the hill surface at $Re_H = 250,000$ in global coordinates. Black circles show LDV profile locations. Black vectors indicate mean flow direction at the wall, while blue vectors indicate mean flow direction at $x_2^+ \approx 500$. (a) Full pressure coefficient contour on the surface. (b) Focus view of the three stations of interest on the bump. Here the pressure coefficient color range is limited to better show the pressure contours in this region.

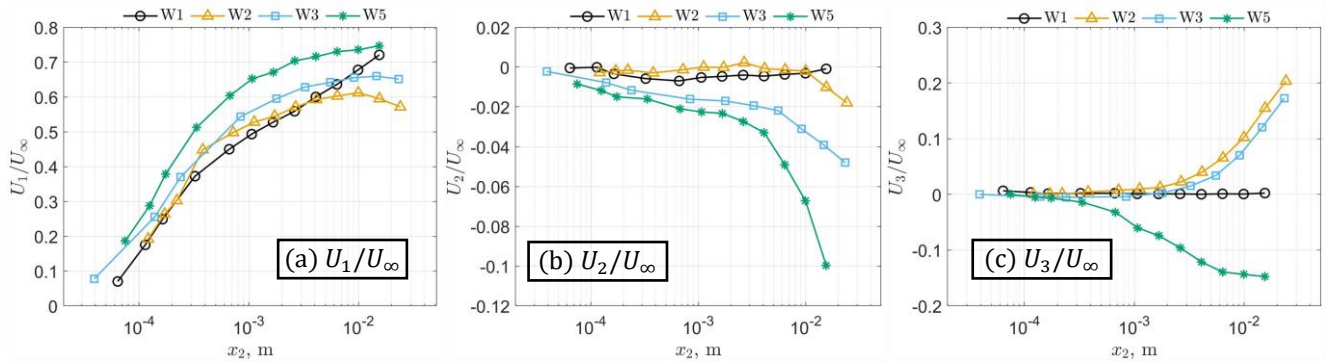


Figure 3. Components of the mean velocity in local wall-shear-stress coordinates, normalized by the freestream velocity. (a) U_1/U_∞ . (b) U_2/U_∞ . (c) U_3/U_∞ .

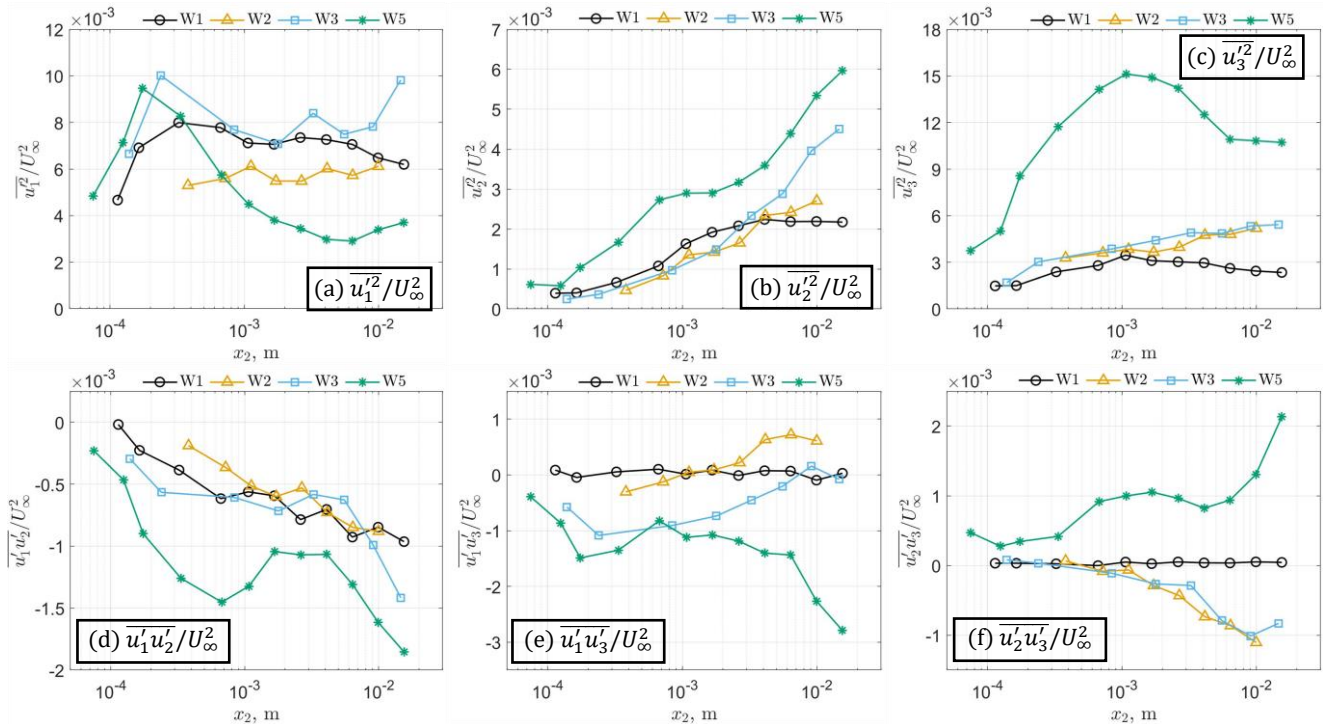


Figure 4. Components of the Reynolds stress in local wall-shear-stress coordinates, normalized by the freestream velocity. (a) $\overline{u_1'^2}/U_\infty^2$. (b) $\overline{u_2'^2}/U_\infty^2$. (c) $\overline{u_3'^2}/U_\infty^2$. (d) $\overline{u_1'u_2'}/U_\infty^2$. (e) $\overline{u_1'u_3'}/U_\infty^2$. (f) $\overline{u_2'u_3'}/U_\infty^2$.

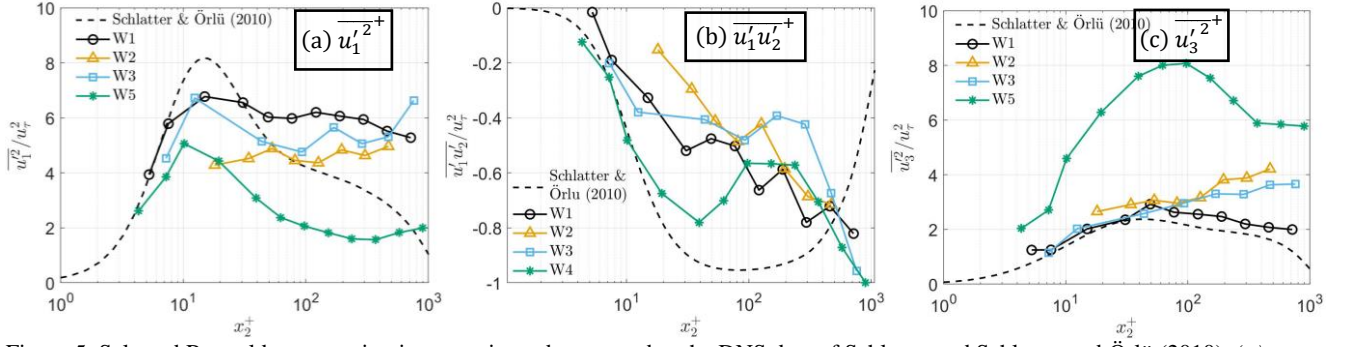


Figure 5. Selected Reynolds stresses in viscous units and compared to the DNS data of Schlatter and Schlatter and Örlü (2010). (a) $\overline{u_1'^2}/u_\tau^2$. (b) $\overline{u_1' u_2'} / u_\tau^2$. (c) $\overline{u_3'^2}/u_\tau^2$.

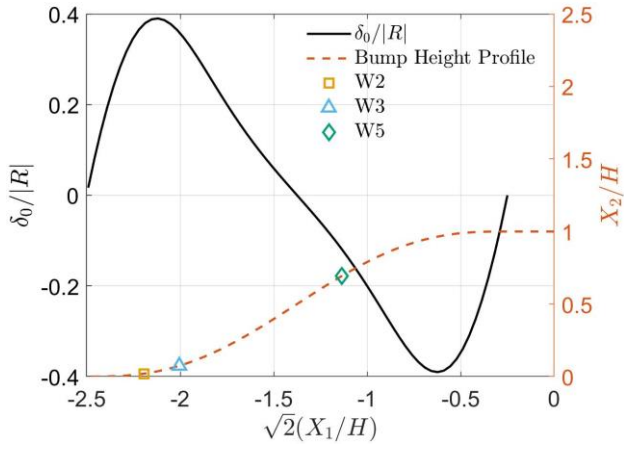


Figure 6. The ratio of the empty tunnel boundary layer thickness at the location of the center of the hill, δ_0 , to the local magnitude of the 3D radius of curvature, $|R|$. $\delta_0/|R| > 0$ indicates concave curvature, while $\delta_0/|R| < 0$ indicates convex curvature. Symbols indicate the location of the hill stations on the local curvature.

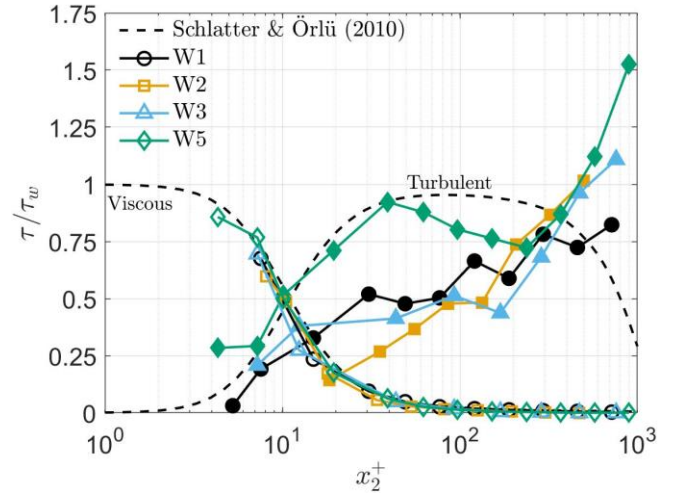


Figure 7. Comparison of viscous and turbulent shear stress components at the four stations of interest, compared to the 2D DNS of Schlatter and Örlü (2010) at $Re_\theta = 4060$. Open symbols indicate viscous stress components, $\partial U_1^+/\partial x_2^+$, and filled symbols indicate turbulent shear stress components, $\sqrt{\overline{u_1' u_2'^2} + \overline{u_2' u_3'^2}}$.

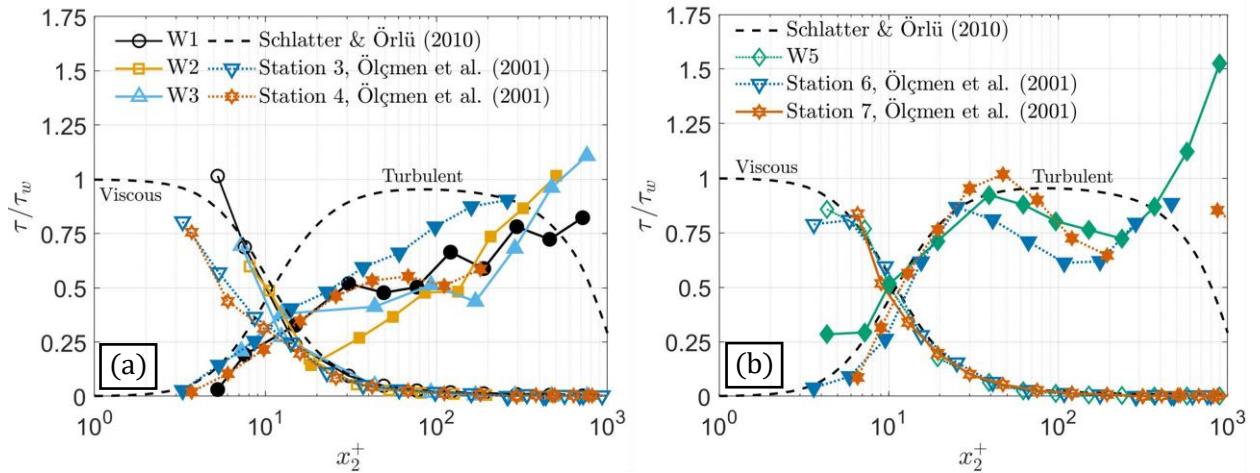


Figure 8. Comparison of turbulent and viscous shear stress behavior of selected stations on the BeVERLI Hill with the 2D equilibrium DNS of Schlatter and Örlü (2010) and the 3D flat-wall TBL of Ölçmen *et al.* (2001). (a) Stations W1, W2, and W3 of the BeVERLI Hill compared with stations 2 and 3 of Ölçmen *et al.* (2001). (b) Station W5 of the BeVERLI Hill compared with stations 6 and 7 of Ölçmen *et al.* (2001).